



# Simultaneous High Speed (5 kHz) Fuel-PLIF, OH-PLIF and Stereo PIV Imaging of Pressurized Swirl-Stabilized Flames using Liquid Fuels

Ianko Chtere<sup>1</sup>, Nicholas Rock<sup>1</sup>, Hanna Ek<sup>1</sup>, Benjamin Emerson<sup>2</sup>, Jerry Seitzman<sup>3</sup> and Timothy Lieuwen<sup>3</sup>  
*Georgia Institute of Technology, Atlanta, GA 30332*

Tonghun Lee<sup>4</sup>  
*University of Illinois, Urbana, IL 61801*

Naibo Jiang<sup>5</sup> and Sukesh Roy<sup>5</sup>  
*Spectral Energies, LLC, Dayton, OH 45431*

James Gord<sup>6</sup>  
*Air Force Research Laboratory, Wright-Patterson AFB, OH 45433*

**This paper describes implementation of simultaneous, high speed (5 kHz) stereo PIV, OH and fuel-PLIF in a pressurized (up to 5.2 atm), liquid fueled, swirl stabilized flame, representative of a gas turbine combustor. The experiments were performed to characterize the flowfield, qualitative heat release and fuel spray distributions, and flame dynamics. Acquiring high speed OH-PLIF in pressurized, liquid fuel systems is difficult due to the fuel's absorption and emission spectra strongly overlapping that of the OH fluorescence spectrum. To overcome the fuel emission polluting the OH signal, the OH and fuel fluorescence signals were partially separated by using two cameras with differing spectral filters and data acquisition timing, as the emission from OH and fuel differ both in spectral width and time. The first camera captured only fuel-PLIF, while the second captured fuel-PLIF and OH-PLIF. The fuel-PLIF images were used to compute two intensity thresholds, separating each image into regions of no fuel, fuel only and an intermediate region. In the region of no fuel, OH was detected in the second camera. In the intermediate region there was a mix of fuel and OH. Instantaneous and time-averaged results are discussed showing the flow field, flame position and dynamics, and spray distribution from the fuel signal for two different multi-component liquid fuels (Jet-A and C-5), at two inlet temperatures of 450 and 570 K, and three pressure of 2.1, 3.5 and 5.2 bar. The flame shape in some cases is described as M-shaped, existing both inside and outside of the annular swirling jet produced by the nozzle, while in other cases no reaction is apparent on the inside. The spray penetration and distribution, and flame position are sensitive to the various conditions, while the flow field topology is qualitatively insensitive. Furthermore, elevated pressure as expected sharpens all spatial gradients in the data.**

<sup>1</sup> Graduate Research Assistant, AIAA Student Member

<sup>2</sup> Research Engineer, Ben T. Zinn Combustion Laboratory, AIAA Member

<sup>3</sup> Professor, School of Aerospace Engineering, AIAA Fellow

<sup>4</sup> Assoc. Prof., Mechanical Science and Engineering, AIAA Member

<sup>5</sup> Senior Research Scientist, AIAA Associate Fellow

<sup>6</sup> Principal Research Chemist, AIAA Fellow

## Nomenclature

$f/D$	= Lens aperture or f- number
$\bar{p}_1$	= probability field of any detectable fuel spray
$\bar{p}_2$	= probability field of fuel spray only
$F$	= Lens focal length
FWHM	= Full width at half maximum
ISL	= Inner shear layer
IRZ	= Inner recirculation zone
OPO	= Optical parametric oscillator
OSL	= Outer shear layer
ORZ	= Outer recirculation zone
PAH	= Polycyclic aromatic hydrocarbons
PIV	= Particle image velocimetry
PLIF	= Planar laser-induced fluorescence
$r, \theta, z$	= Cylindrical polar coordinate system
sPIV	= Stereo particle image velocimetry
$S_m$	= Swirl number
$T_{ph}$	= Preheat temperature of reactants [K]
$U_r$	= Radial flow velocity component [m/s]
$U_z$	= Axial flow velocity component [m/s]
$U_{z,0}$	= Mean axial nozzle exit velocity [m/s]
$U_\theta$	= Azimuthal flow velocity component [m/s]
$\phi$	= Fuel/air equivalence ratio

## I. Introduction

INCREASING emissions and operability demands for gas turbine engines require improved understanding of the multi-phase flow field and heat release distribution. In particular, their emissions and operational limits are influenced by (1) liquid phase fuel distribution, including droplet velocity, sizes, and morphology; (2) gas phase fuel distribution and local fuel/air ratio; (3) gas phase velocity field; (4) heat release; and (5) key scalar species distributions. These quantities can be directly tied to emissions characteristics, such as unburned hydrocarbons, NOx and particulates, as well as operability characteristics, such as combustion instability, ignition, and blowoff. For example, gas phase fuel/air ratio distributions play important role in ignition probabilities, while the axial heat release distribution (which is more fundamentally controlled by liquid fuel distribution, flow velocity, etc.) controls combustion instability limits.

High speed (kHz), spatially resolved imaging techniques provide important insights into these dynamic processes. High speed PIV systems have enabled significant improvements in understanding the morphology of unsteady, three dimensional swirling flows,<sup>1, 2</sup> while high speed PLIF techniques, particularly systems targeting the OH radical, have enabled simultaneous visualizations of the flame zone with high temporal resolution.<sup>3-6</sup>

Significant challenges arise, however, when making measurements in multi-phase (liquid fueled), high pressure, reacting environments. First, the cost and complexity associated with operating high pressure, high power rigs pose challenges in optimizing the setup over multiple iterations. Also, the need to image through multiple optical windows introduces additional issues, such as scattering, window fouling, and optical distortions. These windows, which must be able to withstand the pressurized and high temperature conditions, must also have high transmittance when performing diagnostics in the UV range. In addition, the vibrations and noise of the combustor may require the laser system to be physically separated from the test cell, requiring a longer beam path that is more vulnerable to vibrations. Finally, when doing fluorescence measurements with complex fuels, it is difficult to differentiate regions containing fuel from those containing OH.

This work is a continuation of previous work by the same authors<sup>7</sup> which presented preliminary OH-PLIF and fuel-PLIF measurements with simultaneous sPIV in a high pressure aero-engine type swirler with Jet-A fuel. The previous work noted the need for additional work in delineating and interpreting OH vs. fuel regions, and only discussed results from a limited data set. The present work further improves the fluorescence imaging interpretation (i.e., to differentiate fuel from OH) and presents results from a much larger set of data, including and additional fuel and operating condition.

Many prior workers have reported results from high pressure, liquid-fueled, reacting PIV. Examples of such low repetition rate work are from Hochgreb's group<sup>8,9</sup> and researchers at the DLR Institute of Combustion Technology<sup>10,11</sup>, and high repetition rate from Slabaugh et al.<sup>12,13</sup>

OH-PLIF has been performed at low repetition rates in reacting flow systems with liquid fuel. Allen et al.<sup>14</sup> described measurements on neat fuel sprays (heptane, methanol and ethanol) from 1 to 10 bar, and observed interference from PAH fluorescence. The PAH levels increased with pressure, similar to soot production, as noted in numerous studies.<sup>15,16</sup> Frank et al.<sup>17</sup> presented 10 Hz OH fields at varying global fuel/air ratios and pressures up to 20 bar with liquid fuel. Locke et al. performed 10 Hz OH-PLIF in a swirl-stabilized fuel tube combustor with JP-8 spray at pressures up to 18 bar.<sup>18,19</sup>

Initial work on high-speed OH-PLIF imaging in a liquid-fueled, swirl combustor employed multiple, low repetition-rate lasers to create an eight shot burst at pressures up to 13 bar.<sup>20</sup> With innovations in laser systems, intensifiers, and cameras in recent years, high speed imaging for combustion research has seen a rapid increase using either short bursts of pulses<sup>21,22</sup> or sustained continuous pulse trains.<sup>2,4,5</sup> Examples of continuous high speed high pressure, liquid-fueled, reacting simultaneous PIV and OH-PLIF are the works of Slabaugh et al.<sup>12,13</sup>

The current work focuses on simultaneous high speed sPIV, OH-PLIF, and fuel-emission measurements in high pressure, liquid-fueled, swirling, reacting flows. The main challenges are outlined as follows.

PIV suffers from interference caused by liquid droplet scattering, as the droplets may be brighter than the seeding particles. This produces a measured velocity bias as large droplets do not follow the flow well. Two options are to mask out the region of spray from the PIV fields<sup>10,11</sup> or attempt to separate the spray and seeding particles before PIV processing.<sup>12,13</sup> LIF measurements of OH in high pressure, liquid fuel combustion are practically plagued by:<sup>23-26</sup>

- (1) Reduction of fluorescence yield due to increase in collisional quenching (mitigated somewhat by increase in number density);
- (2) Collisional broadening and overlap of the excitation lines
- (3) Fluorescence trapping due to the increased optical density at high pressure;
- (4) Laser energy absorption by liquid fuel and higher gas concentration;
- (5) Interference from liquid fuel and unburnt hydrocarbon fluorescence resulting from fuel decomposition.

High speed measurements add further complications, as the excitation energy (per pulse) is reduced substantially. A typical high speed dye laser system today has pulse energies in the  $\sim 100\mu\text{J}$  range, compared to  $\sim 10\text{mJ}$  for low speed Nd:YAG-pumped dye lasers and OPO's, and  $\sim 100\text{mJ}$  for tunable excimer lasers.<sup>14</sup> The high pulse energy of the lower repetition rate systems produces better contrast in the fluorescence signal, compensating for the losses associated with fluorescence quenching (1), trapping (2), and laser energy depletion. In practice, the interference from fuel and other hydrocarbons (4) are the most critical issue, as shown in the earlier high speed imaging work in similar flames<sup>20</sup> and require specialized detection and post-processing schemes discussed in this work.

The key contribution of this paper is to give a unique glimpse into the combustion physics of high pressure liquid fuel in an aero engine type combustor by applying simultaneous sPIV, OH-PLIF, and fuel-PLIF. Results are presented at operating pressures of 2-5 bar, with two different liquid fuels, and at low and high  $T_{ph}$ .

## II. Experimental Facility and Diagnostics

### *Combustor Design*

The experimental facility used here (Figure 1) is the same as in refs. [7, 27], with results here from the airblast atomizer only. The facility details are reproduced below. Key components include air supply and preconditioning, fuel supply, the optically accessible pressure vessel and liner, fuel injector, and exhaust section. The facility description is structured with a detailed discussion of each of these processes.

Compressed air at pressures up to 20 atm is heated to temperatures from 350 to 750 K. Following this heating process, a portion of the air is sent to the test section and the remainder is cooled to approximately 320 K in a heat exchanger. This secondary air flows around the liner and keeps the pressure vessel structure and windows cool. Hot combustion products mix with the cooling air downstream of the test section and exit through a water cooled exhaust. A choked orifice plug of variable size is installed at the exhaust exit in order to maintain elevated pressure in the combustion chamber. Air mass flow rates are calculated using a Rosemount vortex flowmeter. The air temperature is measured 350 mm upstream of the dump plane and its value was continuously recorded during measurements. Its value typically remained within  $\pm 10$  K of the nominal value during a measurement. All temperatures are measured with K-type thermocouples. Uncertainties in the nozzle velocity measurement are estimated by propagating errors to be 1.3 % for the lowest nozzle velocity.

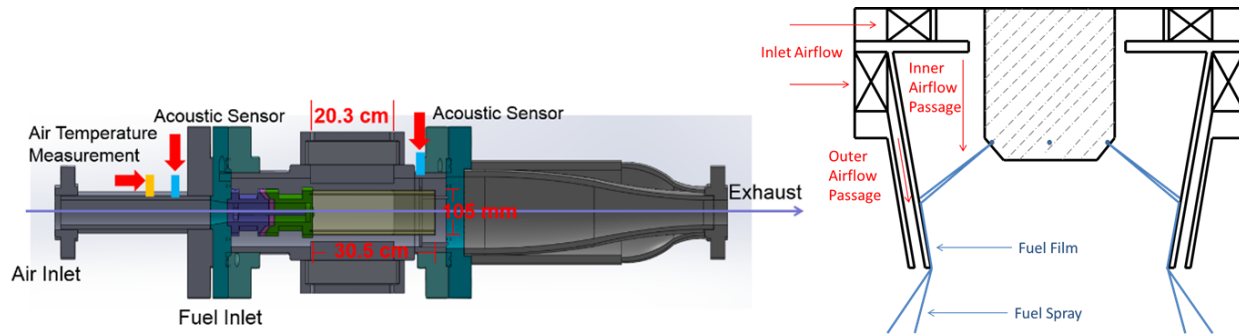


Figure 1: Schematic of combustor (left) and the swirler/fuel injector (right)

The combustor liner consists of a 305 mm long, 105 mm inside diameter quartz section. The front end of the liner, or nozzle outlet, referred to as the “bulkhead” in this paper consists of a stainless steel wall without secondary cooling passages, and is shown in Figure 1 (right). This bulkhead face contains four thermocouples situated flush with the surface for monitoring bulkhead temperature, a static pressure transducer, and an ignitor. Uncertainties in combustor pressure measurements are estimated to be 1.0 % for the lowest pressure.

The pressure vessel that the liner is mounted in has optical access on all four sides, with four quartz windows with dimensions 203 x 108 x 51 mm. These items can be seen in Figure 1. Prior to entering the test section, the pressurized-preheated air passes through the swirler depicted in Figure 1 (right), following a design from Cohen and Rosfjord.<sup>28</sup> As shown in Figure 1 (right), air travels through two separate swirler passages. The air exits the nozzle with an average bulk velocity of 65-85 m/s, depending on operating conditions (see Table 1). The airblast nozzle consists of 6 x 0.18 mm diameter holes that spray radially into the flow.

The fuel of interest was pressurized using nitrogen, and the fuel flow was regulated by adjusting the fuel line pressure using a pressure regulator. Fuel flow rates were measured using an AW-Lake positive displacement gear meter. Fuel temperatures were measured at the fuel inlet depicted in Figure 1 and varied between 300 and 305 K. The estimated uncertainty in overall fuel/air ratio ( $\phi$ ) is 2.5% at the lowest  $\phi$ . In between test conditions, when no liquid fuel was flowing but the combustor was hot, the fuel injector orifices were cooled using nitrogen flow to prevent fuel coking.

The data presented here are at various conditions and with two fuels indicated in the table below. The C-5 fuel is a high aromatics content fuel, with a low boiling point and low viscosity compared to Jet-A.<sup>29</sup>

Table 1: Operating Conditions.

Case	$p$ [atm]	$T_{ph}$ [K]	$\phi$	Nozzle velocity [m/s]	Fuel
1	2.1	450	0.38	78	Jet-A
2	3.7	451	0.38	65	C-5
3	3.4	446	0.61	78	Jet-A
4	3.6	570	0.63	85	Jet-A
5	5.2	459	0.47	75	Jet-A

#### High Speed Stereo PIV Setup

The PIV light source is a dual head, frequency-doubled, diode pumped, solid state, Nd:YLF 527 nm laser, with a 2 mJ pulse energy, pulse duration of about 200 ns, and dual pulse separation of 16  $\mu$ s. A 2.0 mm thick and 75 mm wide laser sheet was formed using a combination of cylindrical lenses. It entered through the top of the combustor and was aligned in the  $r$ - $z$  direction to within 0.5 mm to the combustor centerline as shown in Figure 2. Data are acquired at 5 kHz, 7500 frames at a time. Imaging was performed with Photron SA5 cameras at 10 kHz, at a resolution of 896x848 pixels, equipped with an  $f=100$  mm AT-X M100 Tokina lens set to  $f/D=11$ , and a final resolution of approximately 70  $\mu$ m/pixel. A band-pass filter centered at 527 nm was used to reject flame emission. The cameras were installed in a side-scatter configuration and were angled at about 45 degrees relative to the laser

sheet to provide equal displacement sensitivity in-plane and out-of-plane due to the high swirl number of the flow (see Figure 2), and Scheimpflug adaptors were used. Table 2 lists the imaging optics settings and specifications.

The seeding system consisted of a passive agitation, swirling seeder, which operated with about 5% of total air flow. The 0.5-1.0  $\mu\text{m}$   $\text{TiO}_2$  particles were dried in a 500 K oven for 24 hours before use. Seed was injected about 1.8 m upstream of the nozzle exit plane, to ensure uniform seeding density. The windows were cleaned after each run.

A LaVision dual-plane dot pattern target was used to register the cameras, and LaVision's self-calibration was applied to compensate for slight misalignment between the laser sheet and the registration target facial plane. The PIV images were processed using LaVision DaVis 8.1. Pre-processing included sliding minimum subtraction to reduce background interference and particle size normalization to enhance the PIV code sensitivity. Multiple passes with decreasing interrogation windows sizes starting at  $96 \times 96$  pixels were used, and the final window size weighting function was an optimized non-uniform function. For cases 1 and 2, the final window size was  $32 \times 32$  pixels with an overlap of 75%, yielding a vector spacing of 0.57 mm. For case 3,  $24 \times 24$  pixel final windows with 50% overlap were used, yielding a vector spacing of 0.86 mm.

#### *High Speed OH/fuel-PLIF Setup*

A DPSS Nd:YAG laser was operated at 5 kHz, with a 5 mJ pulse energy, to pump a Sirah Credo tunable dye laser, which was then frequency-doubled to yield a UV pulse energy of 300  $\mu\text{J}$ . The  $\sim 566$  nm output of the dye laser has a specified line width of  $0.08 \text{ cm}^{-1}$ , thus the frequency-doubled output linewidth should be  $\sim 0.11 \text{ cm}^{-1}$ . The UV excitation was tuned to the OH  $Q_1(6)$  transition of the (1,0) vibrational branch in the  $A-X$  system using a test burner, corresponding to a wavelength of 282.93 nm. The Q- branch provides strong fluorescence signals, and the  $Q_1(6)$  line has a weak temperature dependence. The PLIF sheet was aligned to the sPIV sheet, and had the same span, but was about 100  $\mu\text{m}$  thick. The laser sheets were coincident to better than  $1/4$  of the PIV sheet thickness, or 0.5 mm.

The imaging cameras were coupled to a high speed image intensifier and placed normal to the laser sheet on either side of the rig, see Figure 2. Note the cylindrical polar coordinate system ( $r, \theta, z$ ) established in the figure. The intensifier allows for the collection of the UV light while also providing gating control to minimize interference from flame emission. An  $f=45$  mm,  $f/D=1.8$ , UV camera lens was attached to each intensifier, and spectral filters were placed in front of each lens.

The OH and fuel-PLIF cameras used different intensifier gate settings and were equipped with different spectral filters to maximize signal separation, while rejecting the excitation wavelength. As illustrated in Figure 3 (top section), some temporal separation was possible by taking advantage of the longer lived fuel fluorescence relative to shorter lived OH fluorescence. As the excitation duration ( $\sim 10\text{ns}$ ) is on the same order of magnitude as the fluorescence lifetime, and there is overlap between the time of fluorescence and excitation, the intensifier gate began shortly before the laser pulse. To maximize OH-PLIF, the intensifier gate was ended as early as possible without cutting off the OH ( $\sim 10$  ns after the laser pulse center) in order to miss some of the fuel-PLIF tail. On the fuel-PLIF intensifier, the gate was ended 30 ns after the laser pulse center in order to capture all of the fuel fluorescence. Both gates were 40 ns long. Note in Figure 3 that the significant portion of the intensifier gates ahead of the laser pulse has no effect on the fluorescence and was required due to the minimum gate duration limit of the intensifiers ( $\sim 40$  ns).

The spectral separation of the fluorescence signals is illustrated by Figure 3 (middle section). As shown, the laser excitation is narrow-band ( $\sim 0.11 \text{ cm}^{-1}$ ), most of the OH fluorescence is concentrated within a 15 nm band, centered around 308 nm, corresponding to the (0,0) vibrational band, and the fuel fluorescence is broad, coinciding with the OH and extending well into the visible range. A 40 nm FWHM bandpass filter, centered at 320 nm was used in conjunction with a 15 nm FWHM bandpass filter, centered at 315 nm was used to optimize for OH imaging. The narrower filter had significant transmission into the visible spectrum and, thus, required use of the broader filter. A 305 nm Schott glass long-pass filter was used to reject only the excitation light and optimize for the fuel-emission. Since the fuel-emission was much brighter than the OH-PLIF rejection of the OH-fluorescence band was not required. The fuel emission camera captured some emission from the quartz tube in the form of horizontal lines, which are easily subtracted in image pre-processing. The approximate resolution of the camera systems are 117  $\mu\text{m}/\text{pixel}$  for camera C3 and 68  $\mu\text{m}/\text{pixel}$  for C4. Table 2 lists the imaging optics specifications and settings.

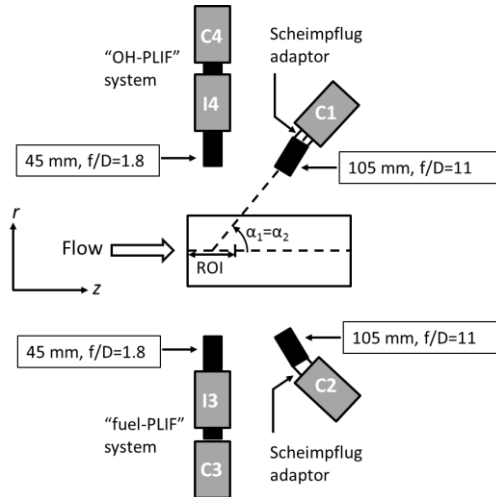


Figure 2: High speed sPIV and 2-Color OH-PLIF camera configuration. C1 and C2 are sPIV cameras, mounted at 45 degrees to laser sheet. C3 is the “fuel-PLIF” camera and C4 is the “OH-PLIF” camera, both coupled to image intensifiers.

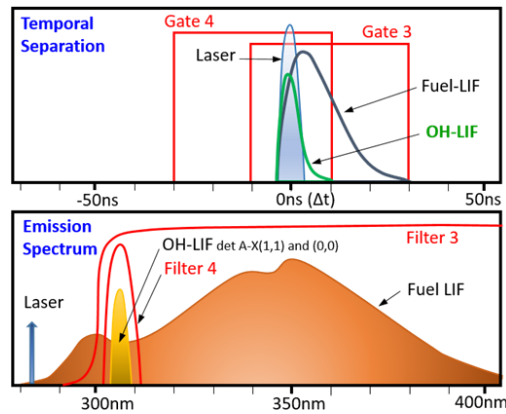


Figure 3: Top: Temporal separation of fuel and OH-LIF signals using intensifiers 3 and 4 gating. Bottom: spectral separation.

Table 2: Imaging optics specifications and settings.

Function	Camera	Intensifier	Intensifier Gate	Lens	Frame Rate/Resolution	f/D Setting	Spectral Filters
sPIV, C1	Photron SA5	N/A	N/A	Tokina AT-X M100 100mm, f/D=2.8	10kHz/896x848 pixels	4.0	Band-pass: 527/20 nm FWHM, T=97%
sPIV, C2	Photron SA5	N/A	N/A	Tokina AT-X M100 100mm, f/D=2.8	10kHz/896x848 pixels	4.0	Band-pass: 527/2 nm FWHM, T=97%
Fuel-PLIF, C3	NAC GX-3	Lambert HICATT (25 mm)	See Fig. 3	Cerco, 45mm, f/D=1.8	5kHz/512x720 pixels	1.8	Long-pass: 2mm Schott WG-305, T=92% above 370 nm, O.D.>3.0 below 280 nm
OH-PLIF, C4	Photron SA1	LaVision IRO (18 mm)	See Fig. 3	Cerco, 45mm, f/D=1.8	5kHz/1024x1024 pixels	1.8	Band-pass: 320nm/40nm FWHM (T=80%) + 315/15 nm FWHM (T=86%), range is up to 500 nm

### III. Data Reduction

This section describes the OH/fuel-PLIF signal separation procedure. Due to absorption of laser energy by the fuel spray the bottom halves of the images have a noticeably lower signal level, and this reduction varies spatially and temporally. Thus, only the top halves are shown in the current work. Due to intrinsic non-linearity in the response of the intensifiers, especially with brighter signals, combined with temporal and spatial variations in the fuel emission spectrum, the fuel image cannot be directly subtracted from the OH + fuel image. We use the fuel-PLIF to instantaneously identify regions of liquid fuel, which is then used to mask those from the OH-PLIF + fuel-

PLIF camera images. We start with synchronized images from the mixed OH-PLIF + fuel-PLIF camera and the fuel-PLIF camera.

First the images from the two flame imaging cameras are corrected for the camera/intensifier/lens system response and laser sheet profile by beginning with a raw image from each camera:

1. Dark image subtraction to compensate for the camera sensor offset at zero light.
2. Flatfield correction for spatial variation in the optical system intensity response.
3. Time-averaged laser sheet intensity correction using acetone-PLIF. Note, however, that we do not correct for the absorption of the laser along its beam path. The bottom halves of the OH/fuel emission images are significantly dimmer due to absorption of the laser energy, and as already mentioned, we only show the top halves.
4. Image registration and LaVision's self-calibration on PIV and PLIF cameras.

Next the fuel and OH + fuel images are post-processed:

1. Figure 4 illustrates the process of subdividing the intensity corrected fuel image into regions of background, OH/fuel overlap, and strong fuel signal, using intensity thresholds extracted from a histogram. An intensity histogram computed for all frames of a given run as shown in Figure 4 reveals two distinct populations, one corresponding to a weak background signal, and one corresponding to the liquid fuel emission signal. Note that it is important to define the ROI for the histogram within the fuel image so that no part of the spray is cropped. In this case we used the entire top half of the interrogation plane. We discuss this in more detail later. The histograms of the fuel images from some cases (Case 1 at 2.1 bar shown in Figure 4), show a second, much less pronounced peak. There is a population of weak signal in some cases, which we will not use here. We speculate that the multimodal distribution of the "signal" portion of the fuel histograms is linked to the atomization physics of the fuel injector. Namely, the weaker signal population may be from a distribution of fine droplets, while the stronger signal may be from a distribution of larger droplets or ligaments. Note that the two (main) populations coexist over a certain region. To determine whether the fuel signal is within the "background", "strong signal" or uncertain region we compute two thresholds which appear naturally from the inflection points of the histogram, as shown in Figure 4. We call the first one the "background cut-off" and the second one the "signal cut-on".

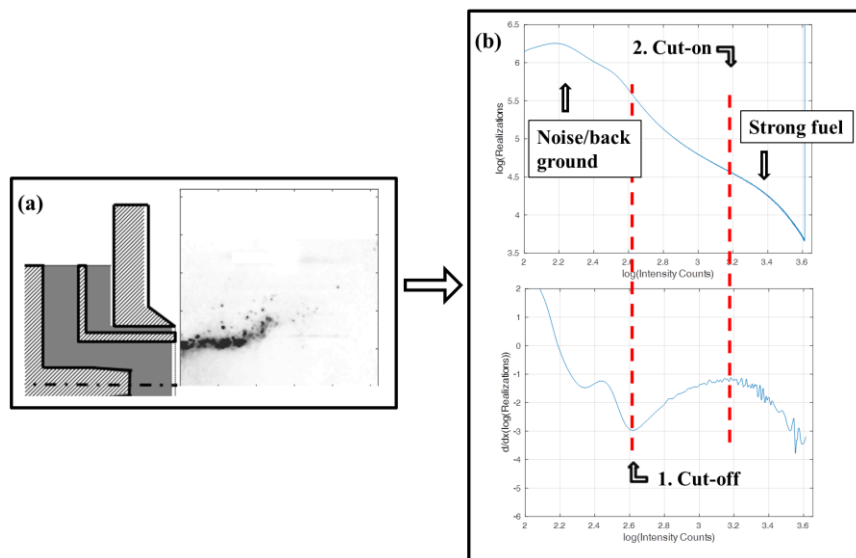


Figure 4: Extracting intensity thresholds from the fuel-PLIF histogram for case 1. (a): fuel-PLIF image. (b): fuel-PLIF intensity histogram from full data set.

2. The process of combining the information from OH and fuel-PLIF is illustrated in Figure 5. Using the thresholds obtained above, we identify three regions within the OH + fuel camera field:

- 1) Intensity is below the "background cut-off", so *there is no detectable fuel* on the fuel-PLIF camera. Therefore any signal on the OH + fuel camera is from OH.
- 2) Intensity is larger than the "background cut-off" threshold, but lower than the "fuel signal cut-on" threshold. There are *smaller droplets and OH* in this region.

3) Intensity is greater than the “fuel signal cut-on” threshold. Therefore, any signal in this region on the OH + fuel camera is dominated by fuel. Furthermore, in the midst of dense regions of spray, we expect no combustion, and therefore, no OH. We conclude there is *only fuel* in this region.

We construct composite false color images as in Figure 5 showing the *fuel only in red*, the *fuel + OH region in purple*, and *no detectable fuel in blue*.

Since the spray intensity varies in time we checked the robustness of the present method by computing and comparing the thresholds for weak spray frames (one standard deviation dimmer than average) and bright spray frames (one standard deviation brighter than average). The resulting thresholds were within 1 mm of each other on the flame images.

#### *Fuel vapor vs. liquid fluorescence contribution*

In the presence of high density spray, the liquid fuel-PLIF greatly overpowers any gaseous fuel PLIF, due to the difference in density. Quenching in the gas phase should be higher in the liquid phase as the quenching molecules cannot penetrate the liquid fuel well. The result is that vapor fuel-PLIF does not register on the camera within the noise/background level. To illustrate the effect of the gaseous to liquid fuel density ratio, consider the vapor to liquid density ratio for Jet-A at 5.2 atm, a vapor temperature of 450 K, and a liquid temperature of 300K, yielding a gas to liquid density ratio of 2.3%. We never expect an interrogation region to be full of 100% vapor fuel, but there are regions of pure liquid, such as the ligaments close to the nozzle lip. Therefore the ratio of mass of fuel in the vapor vs. liquid state would be even lower. Fluorescence scales linearly with the number of molecules, but inversely with the quenching. As mentioned above, quenching will reduce emission ratio below the gas to liquid mass ratio.

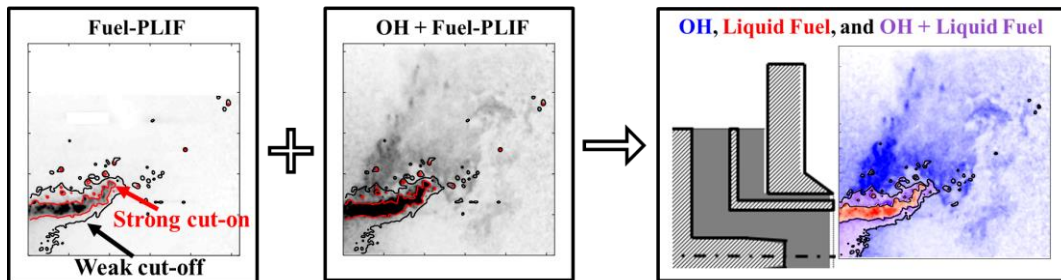


Figure 5: Constructing a false color OH/fuel-PLIF image for case 1. Thresholds lines from Figure 4 are used to split each frame into three regions and create a composite, false color image. Region 1 (red) contains only fuel signal and is taken from the fuel-PLIF camera; region 2 (purple) contains fuel and OH and is taken from the OH/fuel-PLIF camera; region 3 (blue) shows only OH signal.

Although the “OH-PLIF” camera images are not intended to provide OH concentrations, analysis of relative signal values clearly indicates four different signal sources outside of the outer-most (background cut-off) threshold isoline:

- (1) Background signal levels, which are nominally subtracted out in pre-processing above
- (2) A spatially diffuse, low level OH signal in the IRZ/ORZ, due to OH in recirculating product gases. The raw signal levels are roughly 2.3 times larger than the background
- (3) Elevated OH in regions immediately surrounding the fuel jet and in plumes downstream of the flame zone which appear to be closely associated with the reaction zones. The background subtracted raw signal levels are roughly twice higher than the diffuse OH region.

## IV. Results

We next present simultaneous, time-resolved data of 3-component velocity, OH/fuel-PLIF fields at the five operating condition cases as listed in Table 1. As noted above, PLIF images are only shown for the upper half of the flow. Figure 6 illustrates some key swirl flow features for case 1, along with some characteristics of the spray and OH distribution. As illustrated in Figure 5, the red shading denotes fuel only, with signal coming from large droplets and ligaments, while the blue shading outside of the second black contour is signal from OH. The region between the two black contours is where small fuel droplets and OH coexist and cannot be differentiated with this technique.

Indicated in the figure are: (1) fuel spray penetration, (2) swirling annular jet created by the high shear swirler, (3) outer recirculation zone (ORZ), (4) elevated OH level outside and behind the annular jet, (5) helical vortex shedding from the nozzle shear layers (6) centerline reverse flow characteristic of a single cell vortex breakdown, and (7) low OH level inside the annular jet, in the IRZ. Furthermore, the fuel-PLIF reveals the spray distribution, and the OH-PLIF reveals the OH distribution. We will comment further on the fuel and OH distribution in reference to specific cases.

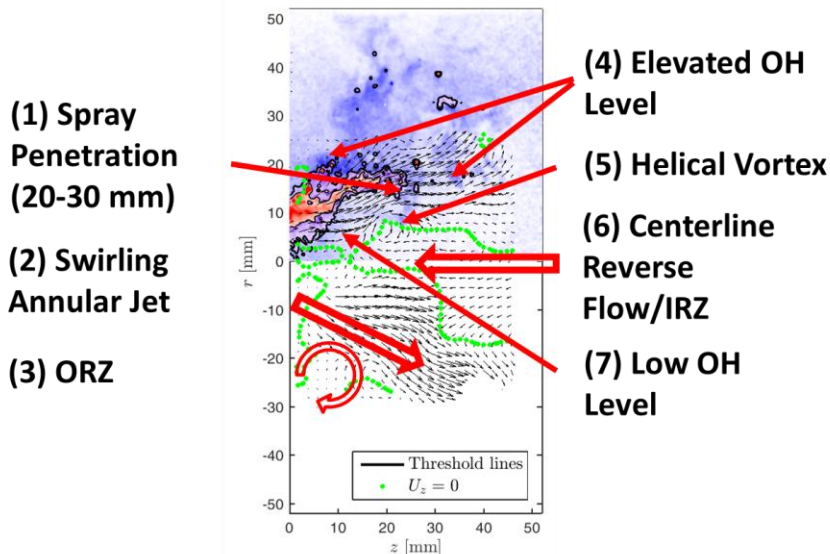


**Figure 6: Overlay of instantaneous flow velocity, OH (blue), fuel (red), and OH+fuel (purple), showing general flow topological features for Case 1**

#### *Pressure comparisons*

Further results for case 1 at the lowest pressure and with a low fuel/air ratio  $\phi=0.38$  are shown in Figure 7 as a filmstrip of 6 consecutive frames  $200 \mu\text{s}$  apart. Each frame consists of part (a): two components of PIV,  $U_z=0$  line in green, and the regions of OH, fuel, and OH+fuel; and part (b): all components of PIV with the out-of-page component color coded, and the  $U_\theta=0$  line in black. In this sequence the highly dynamic nature of the spray is evident. The helical vortex noted in Figure 6 advects axially as the 3-D vortex structure rotates and passes through the laser sheet. In addition to the common features discussed above, the sPIV reveals that the swirling, out-of-plane velocity is highest in this annular jet region, indicating that the jet edges are regions of high shear in both the azimuthal and axial directions. Note that the annular jet region partially overlaps with the fuel spray region, which means that, as mentioned above, the PIV Mie scattering signal is from both seeding particles and fuel droplets. The region of overlap between spray and OH is fairly wide compared to the region of pure spray (and no OH). The OH-PLIF (blue) signal is concentrated outside of the annular jet, in the ORZ. Note, as mentioned before, the presence of both elevated OH signal regions in certain regions (e.g., right outside the fuel jet and downstream of it in the annular jet), as well as a more diffuse background. This elevated OH region is likely the super-equilibrium OH present in the reaction zone, while the diffuse background is likely near equilibrium OH in the combustion products. Elevated OH regions in premixed flames typically occur in the entire region downstream of the flame in the high temperature combustion gases, or at least until these high temperature preproducts are cooled by mixing with other cooling flows. The present fuel lean, low pressure case shows such large uniform regions of elevated OH levels, suggesting premixed combustion. Note also the much weaker or even complete lack of OH-PLIF in the inside of the IRZ or in the center of the flow. This suggests that the flame is wrapped around the outside of the annular fuel jet in this case and that the OH in the center is not associated with combustion, but with recirculating products. As we will discuss next, the flame has a completely different topology in the higher pressure and fuel/air ratio cases. Note, that in premixed fuel and oxidizer combustion systems the flowfield topology strongly affects the flame location, as premixed flames stabilize in the low flow velocity regions created by shear layers and wakes/recirculation zones. Prior work<sup>30</sup> in gaseous flows shows that multiple flame topologies may exist in swirl flows of this nature, with the flame attaching itself to the ISL/OSL of the nozzle, or be stabilized aerodynamically in the center of the flow by vortex breakdown. In the present liquid fuel spray combustion system the flame location and evaporating spray distribution largely interact with each other, but also interact with the gas flow field to a lesser extent compared to a

premixed system. Therefore, the present flame shapes are strongly dictated by the fuel spray characteristics, and do not “anchor” in shear layers. Finally, the flapping motion of the annular jet and spray is evident when comparing the six images.

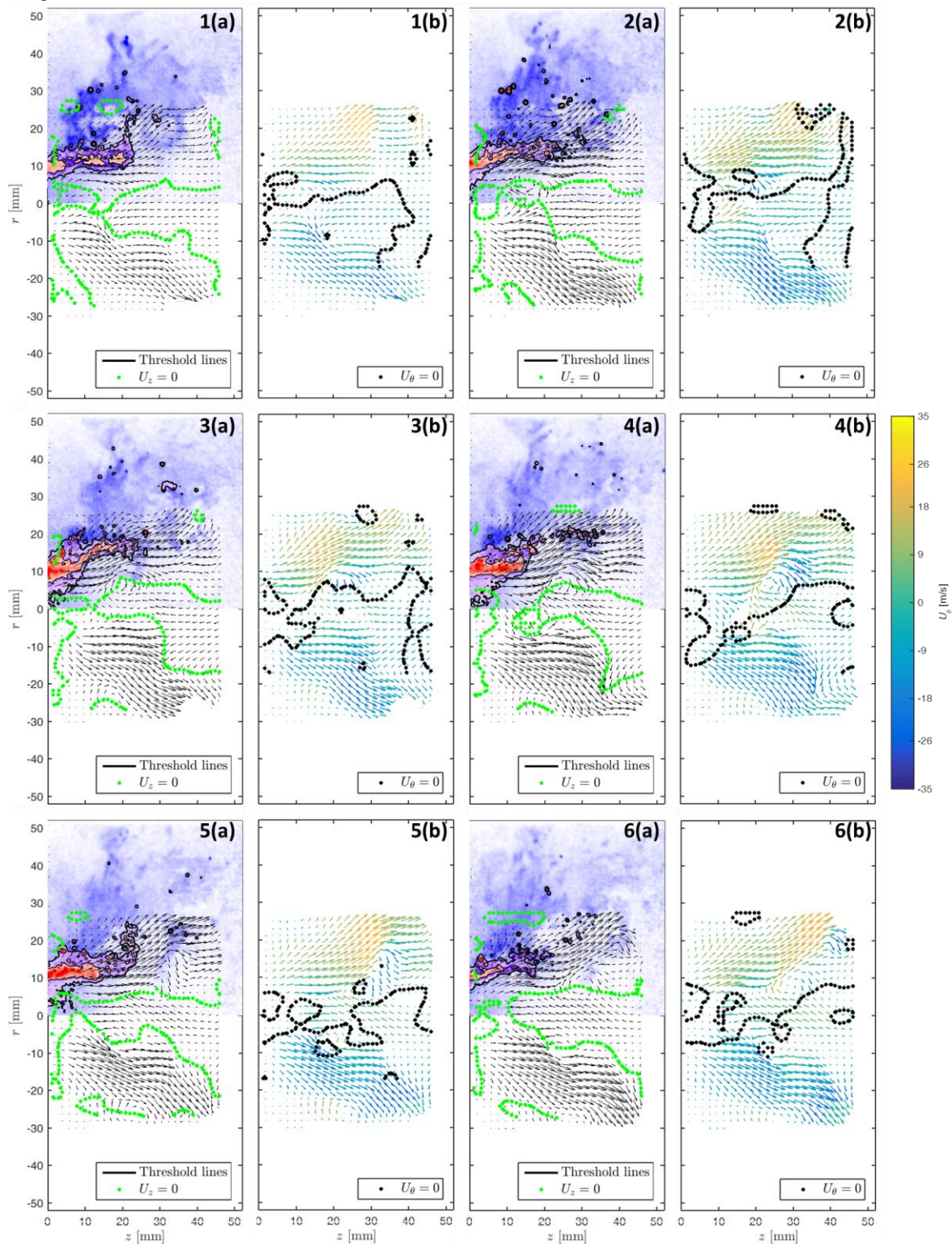
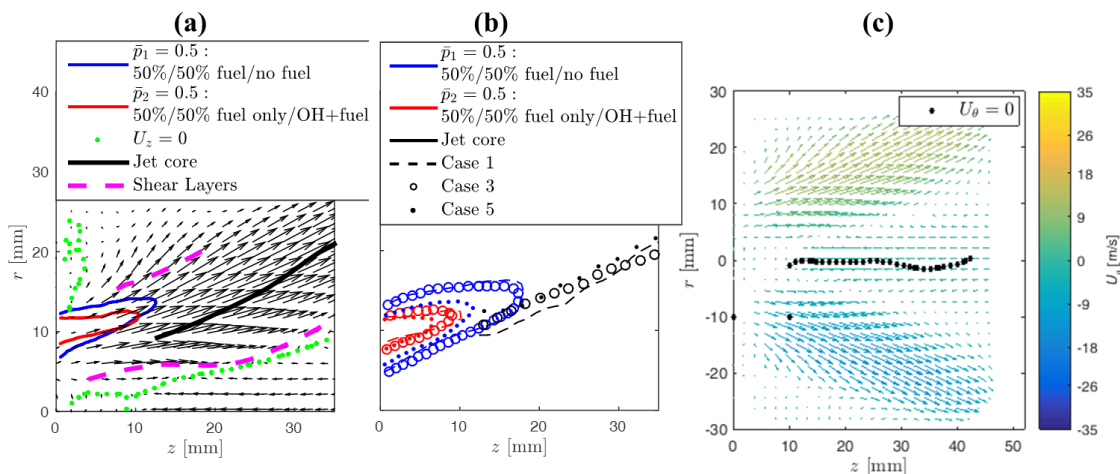


Figure 7: Case 1 instantaneous data. Three frame sequence ( $\Delta t=200 \mu s$ ) of OH-PLIF (blue), fuel-PLIF (red), mixture of fuel and OH (purple) and sPIV in (a). Two components of sPIV are shown in (a) and all three in (b).  $U_z=0$  line plotted in (a) (green) and  $U_\theta=0$  line plotted in (b) (black).

Figure 8 presents the time-averaged velocity field, as well as fuel spray  $\bar{p}_1 = 0.5$  and  $\bar{p}_2 = 0.5$  lines.  $\bar{p}_1$  is the probability field for *detectable* fuel spray, obtained by binarizing the instantaneous field into values of unity for intensities above the background signal threshold (from Figure 4 and Figure 5) and zeros elsewhere, and averaging the binarized images. The  $\bar{p}_1 = 0.5$  line (blue) corresponds to 50% probability of finding detectable fuel. This line can also be thought of as an OH boundary: there is predominantly OH outside. Similarly,  $\bar{p}_2$  is the probability field for finding fuel spray only, obtained by averaged binarized fuel images assigned ones for intensities above the strong fuel threshold and zeros elsewhere. The  $\bar{p}_2 = 0.5$  line (red) corresponds to 50% probability of finding fuel spray only. Although the  $\bar{p}_1$  and  $\bar{p}_2$  probability fields are indicative of the fuel evaporation, they are also affected by the unsteady motion of the spray. Note that there is some OH in the region between  $\bar{p}_1 = 0.5$  and  $\bar{p}_2 = 0.5$ .

The time-averaged in-plane components of PIV along with the  $U_z=0$  line (green) and the  $\bar{p}_1 = 0.5$  (blue) and  $\bar{p}_2 = 0.5$  (red) lines are shown in Figure 8a. The annular jet spreading is indicated by plotting the jet core (locus of maximum velocity magnitude) in black in Figure 8(a). The jet core lines are nearly identical for all cases. The shear layers are also indicated in magenta, as the location of maximum out-of-plane component of vorticity as a function of  $z$ . The  $U_z=0$  line shows the recirculation bubble boundary, and also does not vary much across cases. The  $\bar{p}_2 = 0.5$  contour penetrates about 10 mm, and the  $\bar{p}_1 = 0.5$  contour lies outside of that. Again, the region between  $\bar{p}_1 = 0.5$  and  $\bar{p}_2 = 0.5$  contains fuel and OH, and its thickness is related to the distance between the flame and the bulk of the spray, as well as the unsteady motion of the spray. Figure 8(b) compares the jet cores, and fuel  $\bar{p}_1 = 0.5$  and  $\bar{p}_2 = 0.5$  lines for cases 1, 3 and 5, and will be referred to later. Figure 8(c) plots the time-averaged azimuthal velocity component using a color bar along with the  $U_\theta=0$  line in black. The  $U_\theta=0$  line is along the centerline, as expected, for an axisymmetric time-averaged flow.



**Figure 8: Case 1 time-averaged data and comparison with cases 3 and 5. (a): Two components of sPIV shown along with  $U_z=0$  line (green). Fuel-PLIF  $\bar{p}_2 = 0.5$  line (red) represents 50% probability of finding fuel spray only. Fuel-PLIF  $\bar{p}_1 = 0.5$  line (blue) represents 50% probability of finding any detectable fuel. The jet core (black) and maximum vorticity (magenta) lines are also shown. (b): A comparison of time-averaged jet cores (black),  $\bar{p}_2 = 0.5$  (red) and  $\bar{p}_1 = 0.5$  (blue) lines for cases 1, 3, and 5. (c): All three components of sPIV along with  $U_\theta=0$  line (black).**

Figure 9 plots a representative result for case 3 at a higher 3.5 bar pressure and higher  $\phi=0.61$ . The key qualitative flow field features are the same as in the 2.1 bar, case 1. However, there are numerous differences in the fuel spray and OH distributions. There are elevated OH-PLIF levels also on the inside edge of the fuel jet, as well as outside. These results show that the flame has an “M-flame” structure and surrounds both the outside and the inside of the annular spray. The fact that the flame can stabilize in the IRZ may be a manifestation of the higher fuel/air ratio for this case. Note also the structure of the elevated OH regions which forms a plume downstream of the liquid jet. Both small scale and large scale rollup of the edges of these plumes is evident in the images. Note the pocket at the end of the liquid jet with no OH, presumably consisting of air. The higher pressure is expected to increase

gradients throughout the flowfield, thinning shear layers and flame thicknesses. This is evidenced by a thinning of the elevated OH regions and the overlapping OH and fuel region (purple) compared to the 2.1 bar case. The higher fuel/air ratio of this case is probably responsible for the smaller, broken up OH-containing regions, characteristic of non-premixed combustion. Referring back to Figure 8 (b), the spray penetration distance is similar as the higher fuel flow and the elevated pressure exhibit no net effect. The  $\bar{p}_2 = 0.5$  fuel spray contour for case 3 extends about 9 mm, which is very similar to the 10 mm for case 1 despite the higher fuel/air ratio of 0.61 vs. 0.38 and elevated pressure of 3.4 vs. 2.1 bar. Also evident in Figure 8 (b) is that the OH boundary  $\bar{p}_1 = 0.5$  lines are the same for cases 1 and 3.

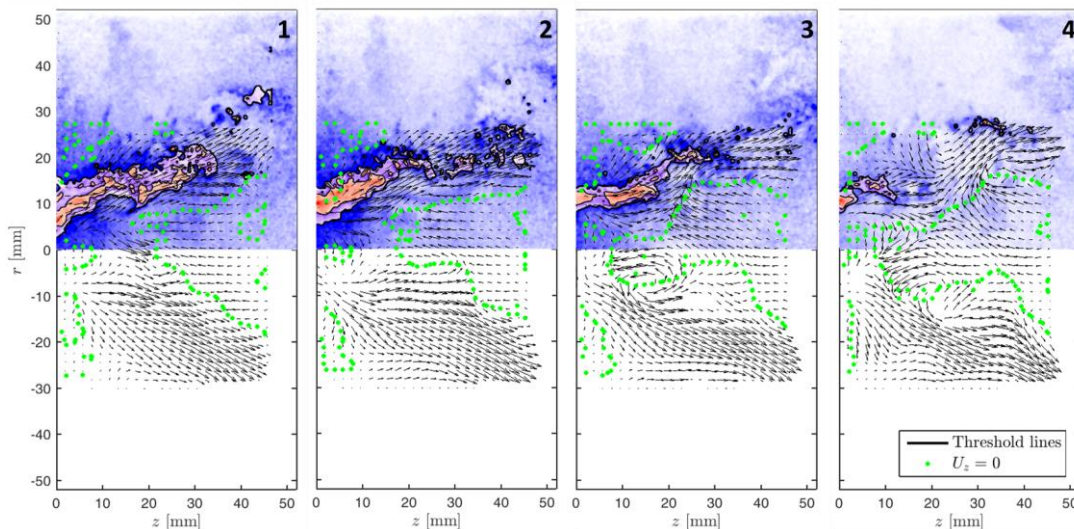


**Figure 9: Case 3 instantaneous data. Three frame sequence ( $\Delta t = 200 \mu s$ ) of OH-PLIF (blue), fuel-PLIF (red), mixture of fuel and OH (purple), and sPIV (black).  $U_z = 0$  line in green.**

Figure 10 presents the 5.2 bar case 5 at an intermediate  $\phi = 0.47$  relative to the two lower pressure cases 1 and 3. The flowfield topology is again qualitatively unchanged. The flame shape is similar to the one from the 3.4 bar, case 3, with OH found both inside outside of the annular jet. The pressure increase is seen to further drive down the spatial extent of the spray, OH, and overlapping spray and OH regions. The OH-containing regions are smaller than in the very lean case 1, but definitely more diffuse than the higher fuel/air ratio case 3, indicating a mixture of premixed and non-premixed combustion. Referring back to Figure 8 (b), we note that the  $\bar{p}_2 = 0.5$  line has shifted upstream and extends only 6 mm, partly caused by the higher pressure and lower  $\phi$  relative to case 3. The OH boundary  $\bar{p}_1 = 0.5$  line is significantly closer to the  $\bar{p}_2 = 0.5$  fuel spray line, and extends only 12 mm relative to 17-18 mm for the lower pressure cases. This increased flame heating of the spray drives further upstream the  $\bar{p}_2 = 0.5$  line.

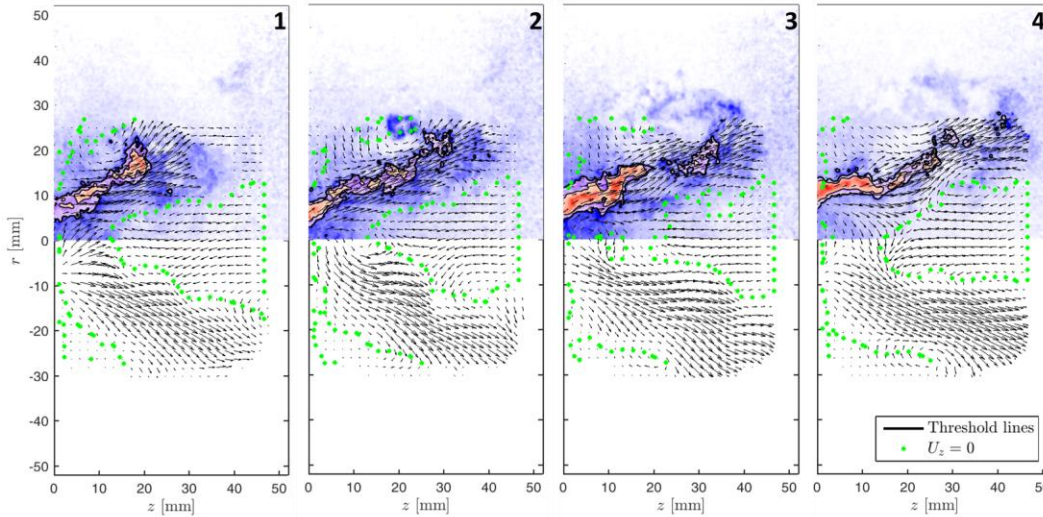


**Figure 10: Case 5 instantaneous data. Three frame sequence ( $\Delta t=200 \mu s$ ) of OH-PLIF (blue), fuel-PLIF (red), mixture of fuel and OH (purple), and sPIV (black).  $U_z=0$  line plotted in green.**

#### *Preheat temperature effects*

We next present the effect of  $T_{ph}$  by studying case 3 (presented above) vs. case 4, the former being at a lower preheat of 450 K and the latter at a higher  $T_{ph}=570$  K. The fuel/air ratios and operating pressures are the same within 5%, while the nozzle velocity at the high preheat is 10% higher. Figure 11 shows three frames from the high preheat case 4. The flowfield again does not change appreciably, but reaction appears predominantly in ORZ, as indicated by OH appearing mostly outside the annular jet. The OH-containing regions are larger and more diffuse as the higher preheat promotes premixed combustion. Figure 12 compares the jet core and fuel spray  $\bar{p}_1 = 0.5$  and OH boundary  $\bar{p}_2 = 0.5$  lines for cases 3 and 4. Everything else being equal, we expect the higher preheat case 4 to show faster evaporation by having a recessed fuel spray  $\bar{p}_2 = 0.5$  line. Instead, we observe the OH boundary line  $\bar{p}_1 = 0.5$  move out axially, from 17 to 20 mm, and radially, from 15 to 19 mm, and the fuel spray only  $\bar{p}_2 = 0.5$  line also move out from 9 mm to 12 mm. There a few competing effects as we increase the preheat temperature and nozzle velocity: First, although the fuel spray only  $\bar{p}_2 = 0.5$  line moves outward, the closer spacing between fuel spray only  $\bar{p}_2$  isolines, i.e.  $\bar{p}_2 = 0.5$  and 0.1 lines (not shown for brevity), indicates the fuel is evaporating faster. As mentioned before the unsteady spray motion may affect the location of these lines further. Second, the faster evaporation likely produces a fuel-rich gas mixture, pushing out the OH boundary  $\bar{p}_1 = 0.5$  line as observed. This in turn would allow the fuel spray  $\bar{p}_2 = 0.5$  line to also move outward as flame heating of the spray would control the distance between the flame and the spray. Third, the higher nozzle velocity would also push the spray and flame outward.

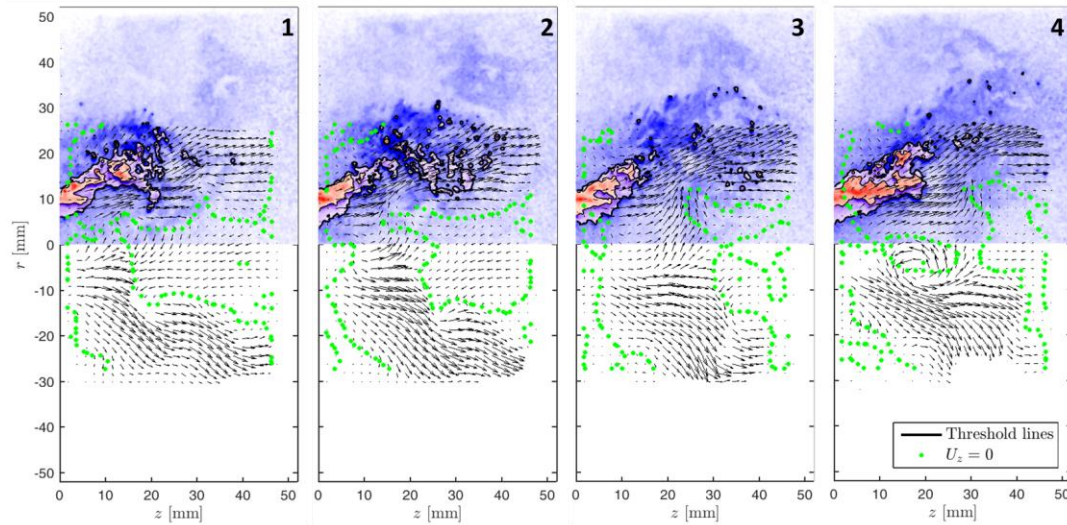


**Figure 11: Case 4 instantaneous data. Three frame sequence ( $\Delta t=200 \mu s$ ) of OH-PLIF (blue), fuel-PLIF (red), mixture of fuel and OH (purple), and sPIV (black).  $U_z=0$  line plotted in green.**

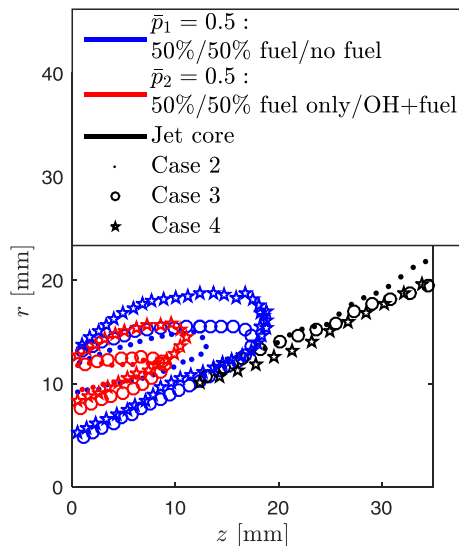


**Figure 12: A comparison of time-averaged data with fuel C-5 for case 2, and at two preheat temperatures for cases 3 and 4. The time-averaged jet cores (black),  $\bar{p}_2 = 0.5$  (red) and  $\bar{p}_1 = 0.5$  (blue) lines are shown.**

#### Observations on C-5

Figure 13 presents case 2, which is at the same pressure and preheat temperature as case 3, but with C-5 and at a lower global  $\phi=0.38$  vs. 0.61. C-5 has a notably lower 90% boiling point of 438 K, relative to 518 K for Jet-A and should evaporate more quickly. Again, there is clear evidence of a plume of higher OH levels downstream, commingled with air and the lower level, more diffuse OH background. This very lean, C-5 fuel case 2 shows a combination of small and large OH-containing regions much like the higher fuel/air ratio case 3 with Jet-A, evidencing again both premixed and non-premixed combustion. This is in contrast with the lean case 1 with Jet-A, which showed high premixing with large diffuse OH-containing regions. Furthermore, there is no flame in the IRZ as in cases 1 and case 4 with Jet-A, and reaction appears predominantly at the ORZ. This flame shape change may be attributed to the lower fuel/air ratio as before, but may also be related to fuel differences. Figure 12 also plots the fuel spray  $\bar{p}_1 = 0.5$  and  $\bar{p}_2 = 0.5$  lines, and the jet core for case 2 in addition to cases 3 and 4. In the present case 2

the global  $\phi$  is much lower resulting in much less spray. Unsurprisingly, the fuel spray  $\bar{p}_1 = 0.5$  and  $\bar{p}_2 = 0.5$  lines move inward relative to cases 3 and 4.

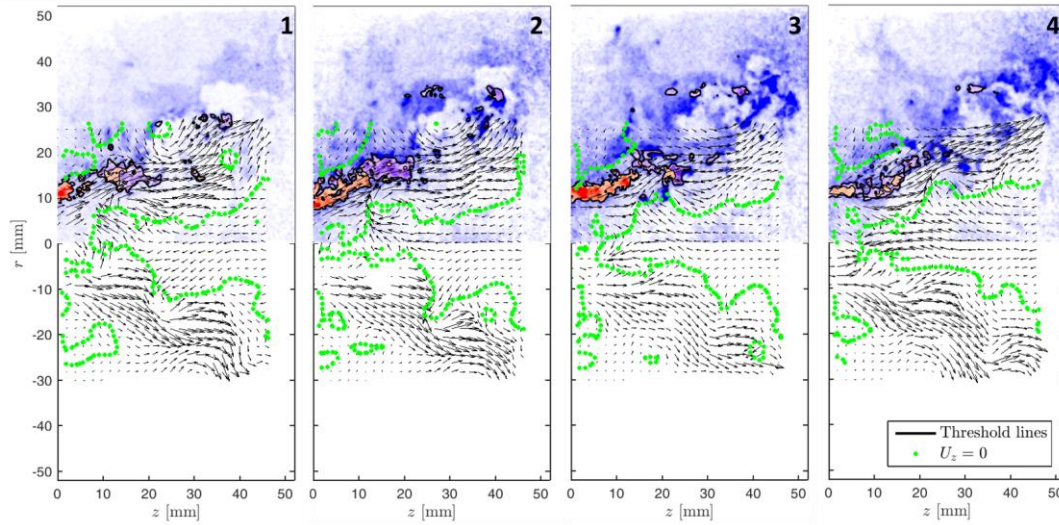


**Figure 13: Case 2 instantaneous data. Three frame sequence ( $\Delta t=200 \mu s$ ) of OH-PLIF (blue), fuel-PLIF (red), mixture of fuel and OH (purple), and sPIV (black).  $U_z=0$  line plotted in green.**

## V. Concluding Remarks

This work has demonstrated a time-resolved (5 kHz) combined OH-PLIF, fuel emission and sPIV in high pressure Jet-A and C-5 spray in a swirl stabilized combustor. A single dye laser is used to excite both the OH and fuel, and the signals are separated spectrally and temporally using two cameras and intensifiers. In order to demonstrate the technique at multiple conditions, measurements were taken with Jet-A and C-5, (C5 has a lower boiling point, higher aromatics content, and lower viscosity), and at different  $T_{ph}=450$  K and 570 K, and pressures of 2.1, 3.5, and 5.2 bar. The resulting data clearly show the spatial extent of the spray, as well as the flame wrapping around the fuel jet. At higher pressure and increased fuel flow the flame has an “M-shape” as it exists both inside and outside of the fuel, but increasing the preheat extinguished the inner portion of the flame. We also observed OH-containing regions that were quite thin and small (suggestive of a nonpremixed flame), as well as much thicker and more uniform (suggestive of either a premixed flame, or the convection of high temperature, OH-laden zones).

In some cases the spray, flame and flowfield sensitivities to pressure and preheat temperature are rather subtle, and future data sets must be taken at closely matched, comparable conditions. Future work will focus on more quantitative analyses of these data, correlating OH-containing regions with velocity field characteristics. This could include out-of-plane velocities that are carrying OH into and out of the field of view, as well as correlating OH region thicknesses normal to the fuel jet with velocity strain fields. Furthermore, the PIV vector fields will be separated into gas phase vs. spray velocity using the fuel-PLIF data.

## APPENDIX – PIV UNCERTAINTY

With a sheet thickness of 2.0 mm, anticipated  $S_m$  on the order of 1, and nozzle velocity of 65 m/s, the loss-of-pairs due to out of plane motion is calculated to be less than about 50%, which is the worst case scenario, at the nozzle exit. This value greatly improves away from the nozzle exit plane as the azimuthal velocity quickly decays. If greater accuracy is required in the highest swirling regions shorter dual pulse separations can be used at the expense of velocity resolution.

Velocity resolution with LaVision’s sub-pixel interpolation capability down to 0.1 of a pixel is 0.45 m/s given by the camera magnification of  $72 \mu m/\text{pixel}$  and pulse separation of  $16 \mu s$ .  $U_z$  loss-of-pairs error is minimized by using multiple passes with decreasing interrogation window size, allowing much longer axial displacements than a single pass algorithm of a typical interrogation window size.

$U_r$  bias due to centrifugal forces is reduced by the relatively high preheat and further in the hot products, and by the use of the small 0.5-1.0 micron particles. Reference calculations for a simple annular swirler geometry can be found in ref. 30.

Following equations 24b and 25 from Mei<sup>31</sup>, the cutoff frequency based on 50% energy following for 0.5-1 micron particles, was calculated to be 4-17 kHz for 450 K preheat. These values increase by a factor of more than 10 in the products due to the much higher kinematic viscosity.

### Acknowledgments

This work was obtained as part of a larger measurement campaign that was funded by the United Technologies Corporation, the US Federal Aviation Administration (FAA) Office of Environment and Energy as a part of ASCENT Project 27A under FAA Award Numbers: 13-C-AJFE-GIT-008 and 13-C-AJFE-UI-013, and the Air Force under AFRL Contract No. FA8650-13-C-2307. The subset of data presented here was obtained with financial support from United Technologies Corporation and the FAA. Any opinions, findings, and conclusions or recommendations expressed in this material are those of the authors and do not necessarily reflect the views of the FAA or other ASCENT Sponsors.

### References

- 1 A. Upatnieks, J. F. Driscoll, and S. L. Ceccio, 'Cinema Particle Imaging Velocimetry Time History of the Propagation Velocity of the Base of a Lifted Turbulent Jet Flame', in *Proc. Combust. Inst.* (2002), pp. 1897-903.
- 2 A. M. Steinberg, J. F. Driscoll, and S. L. Ceccio, 'Measurements of Turbulent Premixed Flame Dynamics Using Cinema Stereoscopic PIV', *Exp. Fluids*, 44 (2008), pp. 985-99.
- 3 M. Tanahashi, S. Murakami, G. M. Choi, Y. Fukuchi, and T. Miyauchi, 'Simultaneous CH-OH PLIF and Stereoscopic PIV Measurements of Turbulent Premixed Flames', in *Proc. Combust. Inst.* (2005), pp. 1665-72.
- 4 C. Arndt, A. Steinberg, I. Boxx, W. Meier, M. Aigner, and C. Carter, 'Flow-Field and Flame Dynamics of a Gas Turbine Model Combustor During Transition Between Thermo-Acoustically Stable and Unstable States', in *Turbo Expo* (2010).
- 5 A. Steinberg, I. Boxx, M. Stöhr, W. Meier, and C. Carter, 'Effects of Flow Structure Dynamics on Thermoacoustic Instabilities in Swirl-Stabilized Combustion', *AIAA*, 50 (2012).
- 6 M. Shimura, T. Ueda, G. M. Choi, M. Tanahashi, and T. Miyauchi, 'Simultaneous Dual-Plane CH PLIF, Single-Plane OH PLIF and Dual-Plane Stereoscopic PIV Measurements in Methane-Air Turbulent Premixed Flames', in *Proc. Combust. Inst.* (2011), pp. 775-82.
- 7 I. Chtereov, N. Rock, H. Ek, T. Smith, B. Emerson, D. R. Noble, E. Mayhew, T. Lee, N. Jiang, S. Roy, J. Seitzman, and T. Lieuwen, 'Reacting Pressurized Spray Combustor Dynamics, Part 2. High Speed Planar Measurements', in *Turbo Expo* (2016).
- 8 C. T. Chong and S. Hochgreb, 'Spray Flame Study Using a Model Gas Turbine Swirl Burner', *Applied Mechanics and Materials*, 316 (2013), pp. 17-22.
- 9 C. T. Chong and S. Hochgreb, 'Spray Flame Structure of Rapeseed Biodiesel and Jet-A1 Fuel', *Fuel*, 115 (2014), pp. 551-58.
- 10 M. Schroll, J. Klinner, L. Lange, and C. Willert, 'Particle Image Velocimetry of Highly Luminescent, Pressurized Combustion Flows of Aero Engine Combustors', in *Int. Symp. on Particle Image Velocimetry* (2013).
- 11 U. Meier, J. Heinze, E. Magens, M. Schroll, C. Hassa, S. Bake, and T. Doerr, 'Optically Accessible Multisector Combustor: Application and Challenges of Laser Techniques at Realistic Operating Conditions', in *Turbo Expo* (2015).
- 12 Carson D. Slabaugh, Andrew C. Pratt, and Robert P. Lucht, 'Simultaneous 5 kHz OH-PLIF/PIV for the study of turbulent combustion at engine conditions', *Applied Physics B*, 118 (2015), pp. 109-30.
- 13 Carson D. Slabaugh, I. Boxx, S. Werner, Robert P. Lucht, and W. Meier, 'Structure and Dynamics of Premixed Swirl Flames at Elevated Power Density', *AIAA*, 54 (2016), pp. 946-61.
- 14 M.G. Allen, K.R. McMagnus, D.M. Sonnenfroh, and P.H. Paul, 'Planar Laser-Induced-Fluorescence Imaging Measurements of OH and Hydrocarbon Fuel Fragments in High-Pressure Spray-Flame Combustion', *Applied Optics*, 34 (1995), p. 6287.
- 15 O. V. Roditcheva and X. S. Bai, 'Pressure Effect on Soot Formation in Turbulent Diffusion Flames', *Chemosphere*, 42 (2001), pp. 811-21.
- 16 Z. Zhang and Q. A. Ezekoye, 'Soot Production Rate Calculations at Elevated Pressure in a Methane-Air Jet Diffusion Flame', *Combust. Sci. Tech.*, 137 (1998), pp. 323-46.
- 17 Jonathan H. Frank, Michael F. Miller, and Mark G. Allen, 'Imaging of Laser-Induced Fluorescence in a High-Pressure Combustor', in *AIAA Paper 99-0773*. (1999).
- 18 R. J. Locke, Y. R. Hicks, R. C. Anderson, and K. A. Ockunzzi, 'OH Imaging in a Lean Burning High-Pressure Combustor', *AIAA*, 34 (1996), pp. 622-24.
- 19 Yolanda R. Hicks, Randy J. Locke, and Robert C. Anderson, 'Optical measurement and visualization in high-pressure high-temperature aviation gas turbine combustors', in *Symp. Applied Photonics* (2000).
- 20 A. Lantz, R. Collin, J. Sjöholm, Z.S. Li, P. Petersson, and M. Aldén, 'High-Speed Fuel/Hydroxyl Radical Imaging in a Gas Turbine Pilot Burner', *AIAA*, 50 (2012), pp. 971-75.

- 21 P. Petersson, J. Olofsson, C. Brackman, H. Seyfried, J. Zetterberg, M. Richter, and A. Dreizler, 'Simultaneous PIV/OH-  
PLIF, Rayleigh Thermometry/OH-PLIF and Stereo PIV Measurements in a Low-Swirl Flame', *Applied Optics*, 49  
(2007), pp. 3928-36.
- 22 J. Hult, U. Meier, W. Meier, A. Harvey, and C. F. Kaminski, 'Experimental Analysis of Local Flame Extinction in a  
Turbulent Jet Diffusion Flame by High Repetition 2-D Laser Techniques and Multi-Scalar Measurements', in *Proc.  
Combust. Inst.* (2005), pp. 701-09.
- 23 J. M. Seitzman and R. K. Hanson, 'Comparison of Excitation Techniques for Quantitative Fluorescence Imaging of  
Reacting Flows', *AIAA*, 31 (1993), pp. 513-19.
- 24 Brett E. Battles and Ronald K. Hanson, 'Laser-Induced Fluorescence Measurements of NO and OH Mole Fraction in  
Fuel-Lean, High-Pressure (1–10 atm) Methane Flames: Fluorescence Modeling and Experimental Validation',  
*Quantitative Spectroscopy and Radiative Transfer*, 54 (1995), pp. 521-37.
- 25 Hideaki Kobayashi, Yasuo Oyachi, and Kaoru Maruta, 'LIF Measurements of Turbulent Premixed Flames in a High  
Pressure Environment', in *Joint Thermal Engineering Conference* (1999).
- 26 G. Singla, P. Scoufflaire, C. Rolon, and S. Candel, 'Planar Laser-Induced Fluorescence of OH in High-Pressure  
Cryogenic LOx/GH 2 Jet Flames', *Combust. Flame*, 144 (2006), pp. 151-69.
- 27 N. Rock, I. Chterev, T. Smith, H. Ek, B. Emerson, D. R. Noble, J. Seitzman, and T. Lieuwen, 'Reacting Pressurized  
Spray Combustor Dynamics, Part 1. Fuel Sensitivities and Blowoff Characterization', in *Turbo Expo* (2016).
- 28 J.M. Cohen and T.J. Rosfjord, 'Influences on the Uniformity of Sprays Produced by gas Turbine High Shear  
Nozzle/Swirlers Assemblies', in *JPC* (1990).
- 29 M. Colket, J. Heyne, M. Rumizen, M. Gupta, A. Jardines, T. Edwards, W. M. Roquemore, G. Andac, R. Boehm, J.  
Zelina, J. Lovett, J. Condevaux, S. Bornstein, N. Rizk, D. Turner, C. Graves, M.S. Anand, R. Williams, F. Xu, J.  
Tishkoff, C. Li, J. Moder, R. Anthenien, D. Friend, P.Chu, R. Kamin, P. Serino, M. Domen, C.M. Kweon, V. Sankaran,  
J. Cohen, and W. Chishty, 'An Overview of the National Jet Fuels Combustion Program', in *SciTech* (2016).
- 30 I. Chterev, C. W. Foley, D. Foti, S. Kostka, A. W. Caswell, N. Jiang, A. Lynch, D. R. Noble, S. Menon, J. M.  
Seitzman, and T. Lieuwen, 'Flame and Flow Topologies in an Annular Swirling Flow', *Combust. Sci. Tech.*, 186  
(2014), pp. 1041-74.
- 31 R. Mei, 'Velocity Fidelity of Flow Tracer Particles', *Exp. Fluids*, 22 (1996), pp. 1-13.